frontiers | Frontiers in Chemistry

TYPE Original Research
PUBLISHED 20 July 2023
DOI 10.3389/fchem.2023.1230187

OPEN ACCESS

EDITED BY
Jianneng Liang,
Shenzhen University, China

REVIEWED BY
Xia Li,
Concordia University, Canada
Yang Zhao,
Western University, Canada
Chuang Yu,
Huazhong University of Science and Technology, China

*CORRESPONDENCE
Lei Gao,
gaolei2018@pku.edu.cn
Songbai Han,
hansb@sustech.edu.cn

†These authors share first authorship

RECEIVED 28 May 2023
ACCEPTED 10 July 2023
PUBLISHED 20 July 2023

CITATION
Di L, Pan J, Gao L, Zhu J, Wang L, Wang X, Su Q, Gao S, Zou R, Zhao Y and Han S (2023), Effect of grain boundary resistance on the ionic conductivity of amorphous xLi$_2$S-(100-x)LiI binary system.
Front. Chem. 11:1230187.
doi: 10.3389/fchem.2023.1230187

Effect of grain boundary resistance on the ionic conductivity of amorphous xLi$_2$S-(100-x)LiI binary system

Longbang Di[1†], Jiangyang Pan[1†], Lei Gao[2*], Jinlong Zhu[1], Liping Wang[1], Xiaomeng Wang[1], Qinqin Su[1], Song Gao[2], Ruqiang Zou[2], Yusheng Zhao[3] and Songbai Han[1*]

[1]Academy for Advanced Interdisciplinary Studies, Southern University of Science and Technology, Shenzhen, China, [2]School of Materials Science and Engineering, Peking University, Beijing, China, [3]Eastern Institute for Advanced Study, Ningbo, China

Solid-state electrolytes (SSEs) hold the key position in the progress of cutting-edge all-solid-state batteries (ASSBs). The ionic conductivity of solid-state electrolytes is linked to the presence of both amorphous and crystalline phases. This study employs the synthesis method of mechanochemical milling on binary xLi$_2$S-(100-x)LiI system to investigate the effect of amorphization on its ionic conductivity. Powder X-ray diffraction (PXRD) shows that the stoichiometry of Li$_2$S and LiI has a significant impact on the amorphization of xLi$_2$S-(100-x)LiI system. Furthermore, the analysis of electrochemical impedance spectroscopy (EIS) indicates that the amorphization of xLi$_2$S-(100-x)LiI system is strongly correlated with its ionic conductivity, which is primarily attributed to the effect of grain boundary resistance. These findings uncover the latent connections between amorphization, grain boundary resistance, and ionic conductivity, offering insight into the design of innovative amorphous SSEs.

KEYWORDS

solid-state electrolytes, ionic conductivity, amorphous, grain boundary resistance, mechanochemical milling

1 Introduction

All-solid-state batteries (ASSBs) offer a viable solution to mitigate the safety concerns of conventional lithium-ions batteries (LIBs), in addition to their potential for exploiting the Li-metal anode with a theoretical specific capacity of 3,860 mAh g^{-1} and electrochemical potential of −3.04 V *versus* the standard hydrogen electrode, thereby enabling a significant enhancement of the energy-density of the batteries (Janek and Zeier, 2016). To make ASSBs practical, it is crucial to advance the development of solid-state electrolytes (SSEs) with exceptional performance (Xia et al., 2019; Abakumov et al., 2020; Zhao et al., 2020). Typical SSEs mainly include sulfide, halide, oxide, and other systems. Sulfide SSEs commonly exhibit high ionic conductivity and good processability, but the low intrinsic electrochemical stability windows (Zhu et al., 2015). Halide SSEs offer high ionic conductivity and compatibility with high voltage cathodes such as $LiCoO_2$, but are not stable with Li-metal anode (Kwak et al., 2022). Oxide SSEs exhibit wide electrochemical stability windows, but feature high interfacial and grain boundary resistance (van den Broek et al., 2016). Each SSE owns distinct properties in terms of ionic conductivity, electrochemical window, and

stability in the air (Kamaya et al., 2011; Manthiram et al., 2017; Yao et al., 2019; Kim et al., 2020; Li et al., 2020; Xu et al., 2023). Notably, ionic conductivity is a vital performance indicator that impacts the application of SSEs (Kwak et al., 2022; Yang and Wu, 2022).

The ionic conductivity of SSEs can be optimized by manipulating lattice structure, element substitution, phase change, amorphization, etc (Asano et al., 2018; Wang et al., 2019; Luo et al., 2021; Kwak et al., 2022; Schweiger et al., 2022; Szczuka et al., 2022). Among these methods, amorphization has gained attention due to the emergence of mechanochemical synthesis methods, which is an effective approach to synthesizing SSEs with lower grain boundary resistance (Dalvi and Shahi, 2004; Morimoto et al., 2004; Kim and Martin, 2006; Enayati and Mohamed, 2014). Representatively, the amorphous Li_2S-P_2S_5 binary system SSEs can be prepared by mechanical milling and exhibit a high ionic conductivity (>10^{-4} S/cm) (Hayashi et al., 2004). In addition, some SSEs such as Li_6PS_5I (Brinek et al., 2020), $Li_2B_4O_7$ (Wohlmuth et al., 2016), Li_2ZrCl_6 (Chen et al., 2021), and Li_3YCl_6 (Asano et al., 2018) show higher ionic conductivity after undergoing amorphization. However, the impact of amorphization on the ionic conductivity varies depending on the specific SSEs system, crystalline structures play a critical role in ionic conductivity for numerous SSEs. (Zhao et al., 2019; Schweiger et al., 2022). For instance, a recent study by Schweiger et al. revealed that $Li_{10}GeP_2S_{12}$ experienced an increase in grain boundary resistance and a decrease in ionic conductivity with increasing milling time against the behavior of other SSEs. The mechanism behind this phenomenon is that defects and site disorder caused by ball milling impede the migration of lithium ions within the lattice (Schweiger et al., 2022). Therefore, it is essential to investigate the impact of amorphization on the grain boundary resistance and ionic conductivity of SSEs, while also elucidating the underlying mechanism.

In this study, the amorphous SSEs of binary $x$$Li_2S$-(100-$x$)LiI ($10 \leq x \leq 90$) were synthesized by mechanical ball-milling method for the first time. PXRD analysis indicates that the amorphization degree of $x$$Li_2S$-(100-$x$)LiI system is significantly influenced by the stoichiometry of Li_2S and LiI. Furthermore, electrochemical impedance spectroscopy (EIS) analysis reveals a strong correlation between the amorphization degree of the $x$$Li_2S$-(100-$x$)LiI system and its ionic conductivity, with the effect of grain boundary resistance being the primary contributing factor. Additionally, the increase of Li_2S content in $x$$Li_2S$-(100-$x$)LiI may restrict the grain boundary impedance reduction caused by amorphization.

2 Materials and methods

2.1 Materials synthesis

The amorphous SSEs of binary $x$$Li_2S$-(100-$x$)LiI ($x$ = 10, 30, 50, 70, 90) were synthesized through a ball milling process. First, the starting materials of Li_2S (Alfa Aesar, 99.9%) and LiI (Energy chemical, 98%) were ground in an agate mortar for 30 min to get the homogeneous mixture. Then, the stoichiometric mixtures of Li_2S and LiI were ball-milled at 500 rpm for 33 h in a grinding jar with ZrO_2 balls using planetary ball mill (Pulverisette 7 PL, Fritsch). The ball-to-powder mass ratio is 20:1 during sample preparation, and each cycle running for 15 min and resting for 5 min. The entire preparation process were carried out under an argon atmosphere (O_2 < 0.1 ppm, H_2O < 0.1 ppm).

2.2 X-ray diffraction measurements

PXRD measurements were conducted at room temperature on an Empyrean diffractometer from Malvern Panalytical using Cu Kα (λ = 1.541,874 Å) and a Bragg–Brentano geometry, for identify the phases of $x$$Li_2S$-(100-$x$)LiI binary system. PXRD data were collected with 2θ ranging from 20° to 90° at a scan rate of 0.14° s^{-1}. Before measurements, each sample was placed on a zero-background sample holder in an Ar-filled glovebox and protected by a Kapton film for the hygroscopicity of $x$$Li_2S$-(100-$x$)LiI.

2.3 Electrochemical impedance spectroscopy measurements

Ionic conductivities of $x$$Li_2S$-(100-$x$)LiI binary system were obtained through EIS measurement. Powder samples of $x$$Li_2S$-(100-$x$)LiI were cold pressed into pellets under 4 tons in an insulative mold, and the pellets were placed between two stainless steel rods served as blocking electrodes. EIS measurement was performed on electrochemical workstation analyzer (AUTOLAB M204) in a frequency range from 1 MHz to 1 Hz with an amplitude of 50 mV. Moreover, the Nyquist curves were fitted by equivalent circuit to obtain the bulk resistance and grain boundary resistance of $x$$Li_2S$-(100-$x$)LiI SSEs.

3 Results and discussion

As presented in Figure 1, the amorphous degree of $x$$Li_2S$-(100-$x$)LiI ($x$ = 10, 30, 50, 70 and 90) system significantly depends on the stoichiometry of Li_2S and LiI. Before ball-milling, all PXRD patterns of $x$$Li_2S$-(100-$x$)LiI exhibit sharp-peak feature, which indicates their good crystallinity (Figure 1A). In contrast, the PXRD patterns of $x$$Li_2S$-(100-$x$)LiI after ball-milling exhibit different degrees of broadening (Figure 1B). Representatively, FWHM of the PXRD peaks in the range of 40°–50° is used here to quantitatively analyze the amorphization degree of $x$$Li_2S$-(100-$x$)LiI binary system (Indris et al., 2000; Sasano et al., 2011; Holder and Schaak, 2019; Londono-Restrepo et al., 2019; Schweiger et al., 2022; Sun et al., 2022). It should be emphasized that the peak positions and FWHM of Li_2S or LiI at x = 10 or 90 are not discernible from the PXRD pattern due to the low content. Surprisingly, different stoichiometric ratios of Li_2S and LiI in $x$$Li_2S$-(100-$x$)LiI lead to obviously different amorphization degrees, even under the same ball-milling conditions. As shown in Figures 1C, D, the FWHM of LiI presents an increasing trend with the increase of Li_2S and changes from 0.239 (x = 10) to 1.124 (x = 70), which demonstrates that the presence of Li_2S can promote the amorphization of LiI. In contrast, the FWHM of Li_2S seems to tend to remain constant as x increases in $x$$Li_2S$-(100-$x$)LiI ($x \geq 50$). Interestingly, the amorphization degree of the $x$$Li_2S$-(100-$x$)$P_2S_5$ binary system is also dependent on the stoichiometric ratios of Li_2S

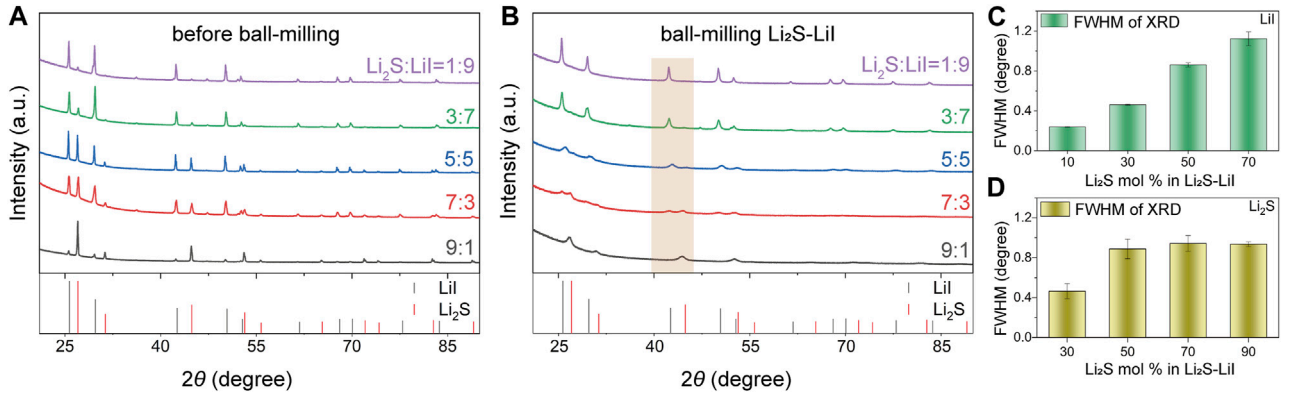

FIGURE 1
PXRD patterns of xLi$_2$S-(100-x)LiI (x = 10, 30, 50, 70 and 90) **(A)** before ball-milling and **(B)** after ball-milling **(C)** FWHM of LiI peak in 40°–45° (x = 10, 30, 50, 70) **(D)** FWHM of Li$_2$S peak in 40°–45° (x = 30, 50, 70, 90).

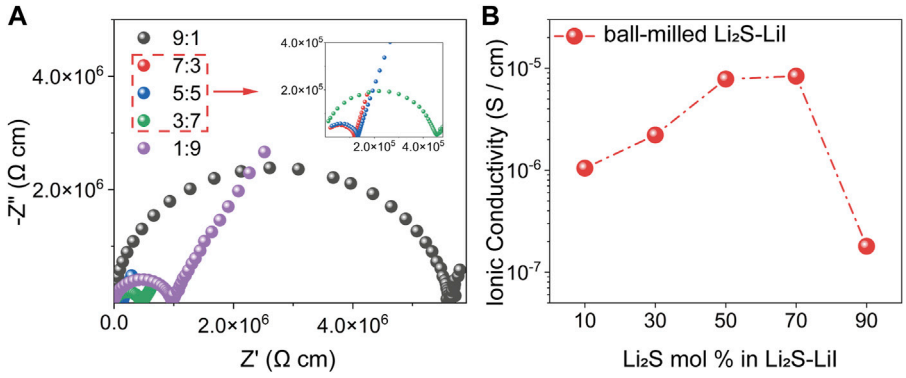

FIGURE 2
(A) Nyquist plots of the amorphous xLi$_2$S-(10-x)LiI **(B)** Ionic conductivities of the amorphous xLi$_2$S-(10-x)LiI.

and P_2S_5 (Minami et al., 2006; Tatsumisago and Hayashi, 2012; Kudu et al., 2018). However, the amorphization degree of xLi$_2$S-(100-x)P_2S_5 diminishes as Li$_2$S increases, accompanied by the appearance of sharp peaks of Li$_2$S in the PXRD patterns (Hayashi et al., 2004). Therefore, the difference between the xLi$_2$S-(100-x)LiI and xLi$_2$S-(100-x)P_2S_5 suggests that the amorphization degree depends not only on the stoichiometric ratios but also on the composition of the compound in the binary system.

The stoichiometric ratios of Li$_2$S and LiI determine the amorphization degree of the xLi$_2$S-(100-x)LiI binary system, which significantly affects its ionic conductivity. Figure 2A shows the Nyquist plots of amorphous xLi$_2$S-(100-x)LiI binary system at room temperature (RT), and each curve exhibits a typical semicircle at high frequency representing the resistance and the linear part at low frequency representing ion blocking electrode. The EIS data were processed based on the formula: $Z = (Z_0 \times S)/l$ to eliminate the effect of SSE pellet thickness and area on the impedance, in which Z_0 is the raw data of the measured EIS, l is the thickness, and S is the area of SSE pellet. Fitting the plot by the equivalent circuit leads to the resistance R, which corresponds to the value of the real part of the Nyquist curve, and the ionic conductivity is calculated according to the formula of $\sigma = l/(R \times S)$. As presented in Figure 2B, the ionic conductivities of xLi$_2$S-(100-x)LiI show a non-monotonic variation with the increase of x. As x increased from 10 to 70, the ionic conductivity of xLi$_2$S-(100-x)LiI increased from 1.03 × 10^{-6} S/cm to 8.43 × 10^{-6} S/cm. Subsequently, after x continued to increase to 90, the ionic conductivity appeared to drop significantly to 1.78 × 10^{-7} S/cm. The above non-monotonic ionic conductivity changes may be attributed to both the amorphization degree of LiI and the content of Li$_2$S in xLi$_2$S-(100-x)LiI. In the first stage (x from 10 to 70), the amorphization of LiI is the dominant factor in influencing the ionic conductivity of xLi$_2$S-(100-x)LiI (Figure 1C). However, in the next stage (x from 70 to 90), the adverse effect of Li$_2$S content on ionic conductivity may play a major role.

To understand the ionic transport mechanism of the amorphous xLi$_2$S-(100-x)LiI in depth, the Nyquist plots were fitted with the equivalent circuit consisting of bulk resistance (R_b), grain boundary

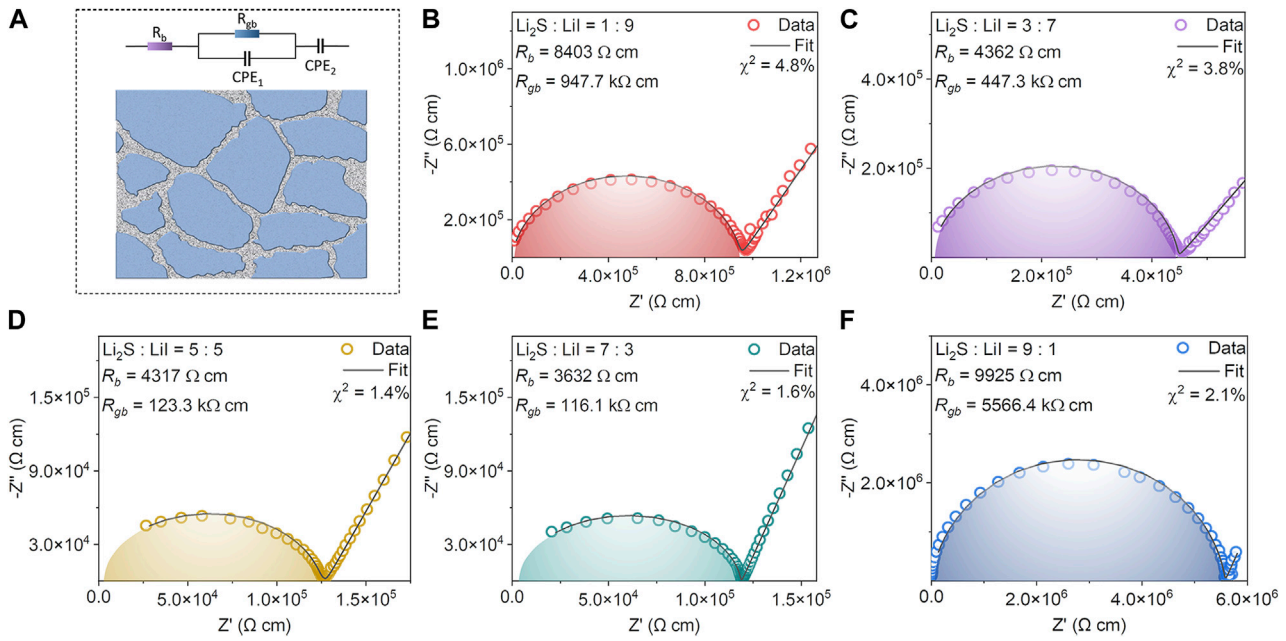

FIGURE 3
(A) Equivalent circuit model for SSEs, consisting of R_b, R_{gb} and CPE. The fitting results of Nyquist plots of **(B)** 10Li_2S-90LiI **(C)** 30Li_2S-70LiI **(D)** 50Li_2S-50LiI **(E)** 70Li_2S-30LiI **(F)** 90Li_2S-10LiI.

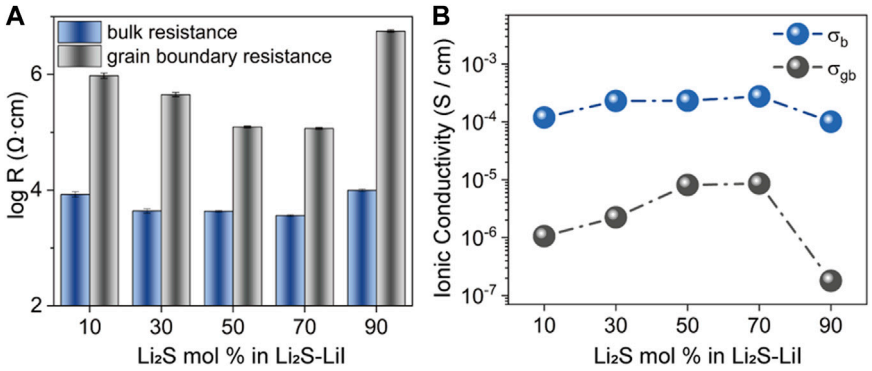

FIGURE 4
(A) Resistance of bulk and grain boundary in xLi_2S-(100-x)LiI. **(B)** Ionic conductivity of bulk and grain boundary in xLi_2S-(100-x)LiI.

resistance (R_{gb}) and constant phase element (CPE). As illustrated in Figure 3A, lithium ions transport in the bulk phase and grain boundary of SSEs, which determines the overall ionic conductivity of xLi_2S-(100-x)LiI (Gao et al., 2016; Goswami and Kant, 2019; Vadhva et al., 2021). Obviously, the hindrance of lithium ions transport at the grain boundaries is stronger than that of the bulk phase according to Figures 3B–F. For 10Li_2S-90LiI, for example, its R_{gb} is 947.7 kΩ cm, which is much higher than that of R_b (8,403 Ω cm). Besides, the variation of R_{gb} is significantly higher than that of R_b. The R_b and R_{gb} of 70Li_2S-30LiI with the highest ionic conductivity are 3,632 Ω cm and 116.1 kΩ cm respectively. In contrast, the R_b and R_{gb} of 90Li_2S-10LiI with the lowest ionic conductivity are 9,925 Ω cm and 5,566.4 kΩ cm respectively.

Furthermore, to present the dependence of R_b and R_{gb} on x in xLi_2S-(100-x)LiI, the differences between R_b and R_{gb} on logarithmic scale are presented in Figure 4A. While the ionic conductivity of xLi_2S-(100-x)LiI undergoes the significant change with x from 10 to 90 (Figure 2), R_b does not undergo a distinct fluctuation, as well as the bulk phase conductivity σ_b. In contrast, R_{gb} and the grain boundary conductivity σ_{gb} show the significant changes and are in agreement with the trend of the ionic conductivity (Figure 4B). Also, the conductivity isotherms extracted from EIS can reflect the

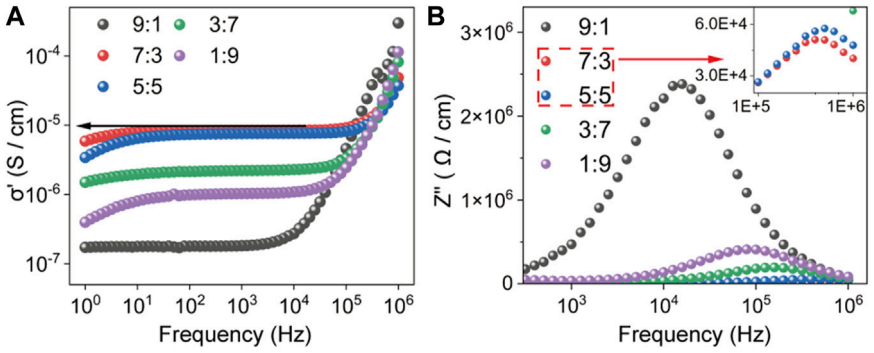

FIGURE 5
(A) The conductivity isotherms of xLi$_2$S-(100-x)LiI **(B)** The imaginary part of the complex impedance of xLi$_2$S-(100-x)LiI.

dependence of the grain boundary conductivity on x in xLi$_2$S-(100-x)LiI, which is consistent with the results of the Nyquist curves fitted with the equivalent circuit. As shown in Figure 5A, conductivity isotherms are plotted from the real part (σ') of the complex ionic conductivity as a function of frequency. Typically, the frequency independent plateaus (marked by arrow) correspond to the ionic conductivities at the grain boundary of SSEs (Schweiger et al., 2022). As x increases, the plateau of σ' gradually reaches a maximum of 8.50×10^{-6} S/cm at $x = 70$, then dropping to a minimum of 1.79×10^{-6} S/cm at $x = 90$. It is worth emphasizing that the feature of conductivity isotherms not only agrees with the analysis of the Nyquist curve, but also the values corresponding to the plateau of σ' are very close to the grain boundary conductivity σ_{gb} in Figure 4B, which confirms the above analysis of ionic conductivity of amorphous xLi$_2$S-(100-x)LiI. In addition, the imaginary part (Z″) of the complex impedance as a function of frequency is plotted in Figure 5B, and the Z″ peak height is usually considered to be equal to half of the most resistive elements (here, i.e., the grain boundary resistance) in SSEs (Irvine et al., 1990). Consistently, the dependence of Z″ peak height on x can also corroborate the results of Nyquist curves fitted with the equivalent circuit.

Obviously, the above results indicate that the ionic conductivity change of amorphous xLi$_2$S-(100-x)LiI depends directly on the grain boundary conductivity σ_{gb} and is almost unaffected by the bulk phase conductivity σ_b. On the other hand, in combination with the PXRD data of xLi$_2$S-(100-x)LiI (Figure 1), it can be concluded that the increase in grain boundary conductivity σ_{gb} may depend on the enhanced amorphization of LiI as x increases from 10 to 70, while the decrease in grain boundary conductivity σ_{gb} may be mainly affected by the increase in Li$_2$S content as x increases from 70 to 90. In other words, there is a competitive relationship between the amorphization of LiI and the content of Li$_2$S in affecting the grain boundary conductivity of amorphous xLi$_2$S-(100-x)LiI.

4 Conclusion

In conclusion, the amorphous xLi$_2$S-(100-x)LiI ($10 \leq x \leq 90$) binary system was synthesized by mechanical ball-milling method. The PXRD analysis significantly demonstrated that the increase of Li$_2$S content can promote the amorphization of LiI, and the amorphous degree of Li$_2$S tend to remain constant as x increases in xLi$_2$S-(100-x)LiI ($x \geq 50$). The EIS analysis revealed that the change in ionic conductivity of amorphous xLi$_2$S-(100-x)LiI depends on the grain boundary conductivity and is almost unaffected by the bulk phase conductivity. In addition, the competitive mechanism between the amorphization of LiI and the content of Li$_2$S in affecting the grain boundary conductivity was found. The findings of xLi$_2$S-(100-x)LiI binary system provide insights into the future design of new amorphous SSEs.

Data availability statement

The raw data supporting the conclusion of this article will be made available by the authors, without undue reservation.

Author contributions

SH and LG designed the project. LD carried out the experiments; LG and LD performed the electrochemical properties and analyzed all the data. LG and JP wrote the manuscript. All authors contributed to the article and approved the submitted version.

Acknowledgments

This work was supported by the open research fund of Songshan Lake Materials Laboratory (2022SLABFK04), the Shenzhen Foundation Research Fund granted by the Shenzhen Science and Technology Innovation Committee (JCYJ20220530112812028), National Natural Science Foundation of China (No. 52227802, 12275119, U22A20439), Major Technologies R & D Program of Shenzhen (JSGGZD20220822095600001), Guangdong Grants (2021ZT09C064), Shenzhen Science and Technology Program (KQTD20200820113047086). The authors thank the support from the Shenzhen Key Laboratory of Solid State Batteries, the Guangdong Provincial Key Laboratory of Energy Materials for Electric Power, the Guangdong-Hong Kong-Macao Joint Laboratory for Photonic-Thermal-Electrical Energy Materials and Devices, Major Science and Technology Infrastructure Project of Material Genome Big-science Facilities Platform supported by Municipal Development and Reform Commission of Shenzhen.

Conflict of interest

The authors declare that the research was conducted in the absence of any commercial or financial relationships that could be construed as a potential conflict of interest.

Publisher's note

All claims expressed in this article are solely those of the authors and do not necessarily represent those of their affiliated organizations, or those of the publisher, the editors and the reviewers. Any product that may be evaluated in this article, or claim that may be made by its manufacturer, is not guaranteed or endorsed by the publisher.

Supplementary material

The Supplementary Material for this article can be found online at: https://www.frontiersin.org/articles/10.3389/fchem.2023.1230187/full#supplementary-material

References

Abakumov, A. M., Fedotov, S. S., Antipov, E. V., and Tarascon, J.-M. (2020). Solid state chemistry for developing better metal-ion batteries. *Nat. Commun.* 11 (1), 4976. doi:10.1038/s41467-020-18736-7

Asano, T., Sakai, A., Ouchi, S., Sakaida, M., Miyazaki, A., and Hasegawa, S. (2018). Solid halide electrolytes with high lithium-ion conductivity for application in 4 V class bulk-type all-solid-state batteries. *Adv. Mat.* 30 (44), e1803075. doi:10.1002/adma.201803075

Brinek, M., Hiebl, C., and Wilkening, H. M. R. (2020). Understanding the origin of enhanced Li-ion transport in nanocrystalline argyrodite-type Li(6)PS(5)I. *Chem. Mat.* 32 (11), 4754–4766. doi:10.1021/acs.chemmater.0c01367

Chen, S., Yu, C., Chen, S., Peng, L., Liao, C., Wei, C., et al. (2021). Enabling ultrafast lithium-ion conductivity of Li2ZrCl6 by indium doping. *Chin. Chem. Lett.* 33, 4635–4639. doi:10.1016/j.cclet.2021.12.048

Dalvi, A., and Shahi, K. (2004). Formation of superionically conducting amorphous phase in mechanically-milled AgI–Ag2O–V2O5 system. *J. Non-Crystalline Solids* 341 (1-3), 124–132. doi:10.1016/j.jnoncrysol.2004.05.004

Enayati, M. H., and Mohamed, F. A. (2014). Application of mechanical alloying/milling for synthesis of nanocrystalline and amorphous materials. *Int. Mat. Rev.* 59 (7), 394–416. doi:10.1179/1743280414y.0000000036

Gao, J., Zhao, Y.-S., Shi, S.-Q., and Li, H. (2016). Lithium-ion transport in inorganic solid state electrolyte. *Chin. Phys. B* 25 (1), 018211. doi:10.1088/1674-1056/25/1/018211

Goswami, N., and Kant, R. (2019). Theory for impedance response of grain and grain boundary in solid state electrolyte. *J. Electroanal. Chem.* 835, 227–238. doi:10.1016/j.jelechem.2019.01.035

Hayashi, A., Hama, S., Morimoto, H., Tatsumisago, M., and Minami, T. (2004). Preparation of Li2S–P2S5 amorphous solid electrolytes by mechanical milling. *J. Am. Ceram. Soc.* 84, 477–479. doi:10.1111/j.1151-2916.2001.tb00685.x

Holder, C. F., and Schaak, R. E. (2019). Tutorial on powder X-ray diffraction for characterizing nanoscale materials. *ACS Nano* 13 (7), 7359–7365. doi:10.1021/acsnano.9b05157

Indris, S., Bork, D., and Heitjans, P. (2000). Nanocrystalline oxide ceramics prepared by high-energy ball milling. *J. Mat. Synth. Process.* 8 (3), 245–250. doi:10.1023/A:1011324429011

Irvine, J. T. S., Sinclair, D. C., and West, A. R. (1990). Electroceramics: Characterization by impedance spectroscopy. *Adv. Mat.* 2 (3), 132–138. doi:10.1002/adma.19900020304

Janek, J., and Zeier, W. G. (2016). A solid future for battery development. *Nat. Energy* 1 (9), 16141. doi:10.1038/nenergy.2016.141

Kamaya, N., Homma, K., Yamakawa, Y., Hirayama, M., Kanno, R., Yonemura, M., et al. (2011). A lithium superionic conductor. *Nat. Mater.* 10 (9), 682–686. doi:10.1038/nmat3066

Kim, A., Woo, S., Kang, M., Park, H., and Kang, B. (2020). Research progresses of garnet-type solid electrolytes for developing all-solid-state Li batteries. *Front. Chem.* 8, 468. doi:10.3389/fchem.2020.00468

Kim, Y., and Martin, S. (2006). Ionic conductivities of various GeS2-based oxy-sulfide amorphous materials prepared by melt-quenching and mechanical milling methods. *Solid State Ionics* 177 (33-34), 2881–2887. doi:10.1016/j.ssi.2006.09.001

Kudu, Ö. U., Famprikis, T., Fleutot, B., Braida, M.-D., Le Mercier, T., Islam, M. S., et al. (2018). A review of structural properties and synthesis methods of solid electrolyte materials in the Li2S– P2S5 binary system. *J. Power Sources* 407, 31–43. doi:10.1016/j.jpowsour.2018.10.037

Kwak, H., Wang, S., Park, J., Liu, Y., Kim, K. T., Choi, Y., et al. (2022). Emerging halide superionic conductors for all-solid-state batteries: Design, synthesis, and practical applications. *ACS Energy Lett.* 7, 1776–1805. doi:10.1021/acsenergylett.2c00438

Li, X., Liang, J., Yang, X., Adair, K. R., Wang, C., Zhao, F., et al. (2020). Progress and perspectives on halide lithium conductors for all-solid-state lithium batteries. *Energy Environ. Sci.* 13 (5), 1429–1461. doi:10.1039/c9ee03828k

Londono-Restrepo, S. M., Jeronimo-Cruz, R., Millan-Malo, B. M., Rivera-Munoz, E. M., and Rodriguez-Garcia, M. E. (2019). Effect of the nano crystal size on the X-ray diffraction patterns of biogenic hydroxyapatite from human, bovine, and porcine bones. *Sci. Rep.* 9 (1), 5915. doi:10.1038/s41598-019-42269-9

Luo, X., Wu, X., Xiang, J., Cai, D., Li, M., Wang, X., et al. (2021). Heterovalent cation substitution to enhance the ionic conductivity of halide electrolytes. *ACS Appl. Mat. Interfaces* 13 (40), 47610–47618. doi:10.1021/acsami.1c13295

Manthiram, A., Yu, X., and Wang, S. (2017). Lithium battery chemistries enabled by solid-state electrolytes. *Nat. Rev. Mater.* 2 (4), 16103–16116. doi:10.1038/natrevmats.2016.103

Minami, T., Hayashi, A., and Tatsumisago, M. (2006). Recent progress of glass and glass-ceramics as solid electrolytes for lithium secondary batteries. *Solid State Ionics* 177 (26-32), 2715–2720. doi:10.1016/j.ssi.2006.07.017

Morimoto, H., Yamashita, H., Tatsumisago, M., and Minami, T. (2004). Mechanochemical synthesis of new amorphous materials of 60Li2S·40SiS2 with high lithium ion conductivity. *J. Am. Ceram. Soc.* 82 (5), 1352–1354. doi:10.1111/j.1151-2916.1999.tb01923.x

Sasano, J., Motomura, K., Nagai, M., Mohamad, F. B., and Izaki, M. (2011). Pulse electrodeposition of CuO thin films to improve crystallinity for the enhancement of photoelectrochemical response. *Electrochem. (Tokyo)* 79 (10), 831–837. doi:10.5796/electrochemistry.79.831

Schweiger, L., Hogrefe, K., Gadermaier, B., Rupp, J. L. M., and Wilkening, H. M. R. (2022). Ionic conductivity of nanocrystalline and amorphous Li10GeP2S12: The detrimental impact of local disorder on ion transport. *J. Am. Chem. Soc.* 144 (22), 9597–9609. doi:10.1021/jacs.1c13477

Sun, C. C., You, A. H., and Teo, L. L. (2022). XRD measurement for particle size analysis of PMMA polymer electrolytes with SiO2. *Int. J. Technol.* 13 (6), 1336. doi:10.14716/ijtech.v13i6.5927

Szczuka, C., Karasulu, B., Groh, M. F., Sayed, F. N., Sherman, T. J., Bocarsly, J. D., et al. (2022). Forced disorder in the solid solution Li3P-Li2S: A new class of fully reduced solid electrolytes for lithium metal anodes. *J. Am. Chem. Soc.* 144 (36), 16350–16365. doi:10.1021/jacs.2c01913

Tatsumisago, M., and Hayashi, A. (2012). Superionic glasses and glass–ceramics in the Li2S–P2S5 system for all-solid-state lithium secondary batteries. *Solid State Ionics* 225, 342–345. doi:10.1016/j.ssi.2012.03.013

Vadhva, P., Hu, J., Johnson, M. J., Stocker, R., Braglia, M., Brett, D. J. L., et al. (2021). Electrochemical impedance spectroscopy for all-solid-state batteries: Theory, methods and future outlook. *ChemElectroChem* 8 (11), 1930–1947. doi:10.1002/celc.202100108

van den Broek, J., Afyon, S., and Rupp, J. L. M. (2016). Interface-engineered all-solid-state Li-ion batteries based on garnet-type fast Li^+ conductors. *Adv. Energy Mater.* 6 (19). doi:10.1002/aenm.201600736

Wang, S., Bai, Q., Nolan, A. M., Liu, Y., Gong, S., Sun, Q., et al. (2019). Lithium chlorides and bromides as promising solid-state chemistries for fast ion conductors with good electrochemical stability. *Angew. Chem. Int. Ed. Engl.* 58 (24), 8039–8043. doi:10.1002/anie.201901938

Wohlmuth, D., Epp, V., Stanje, B., Welsch, A.-M., Behrens, H., Wilkening, M., et al. (2016). High-energy mechanical treatment boosts ion transport in nanocrystalline Li2B4O7. *J. Am. Ceram. Soc.* 99 (5), 1687–1693. doi:10.1111/jace.14165

Xia, S., Wu, X., Zhang, Z., Cui, Y., and Liu, W. (2019). Practical challenges and future perspectives of all-solid-state lithium-metal batteries. *Chem* 5 (4), 753–785. doi:10.1016/j.chempr.2018.11.013

Xu, Y., Zhao, R., Gao, L., Gao, T., Wang, W., Bian, J., et al. (2023). A fiber-reinforced solid polymer electrolyte by *in situ* polymerization for stable lithium metal batteries. *Nano Res.* doi:10.1007/s12274-023-5480-x

Yang, H., and Wu, N. (2022). Ionic conductivity and ion transport mechanisms of solid-state lithium-ion battery electrolytes: A review. *Energy Sci. Eng.* 10 (5), 1643–1671. doi:10.1002/ese3.1163

Yao, P., Yu, H., Ding, Z., Liu, Y., Lu, J., Lavorgna, M., et al. (2019). Review on polymer-based composite electrolytes for lithium batteries. *Front. Chem.* 7, 522. doi:10.3389/fchem.2019.00522

Zhao, Q., Stalin, S., Zhao, C.-Z., and Archer, L. A. (2020). Designing solid-state electrolytes for safe, energy-dense batteries. *Nat. Rev. Mat.* 5 (3), 229–252. doi:10.1038/s41578-019-0165-5

Zhao, W., Yi, J., He, P., and Zhou, H. (2019). Solid-state electrolytes for lithium-ion batteries: Fundamentals, challenges and perspectives. *Electrochem. Energy Rev.* 2 (4), 574–605. doi:10.1007/s41918-019-00048-0

Zhu, Y. Z., He, X. F., and Mo, Y. F. (2015). Origin of outstanding stability in the lithium solid electrolyte materials: Insights from thermodynamic analyses based on first-principles calculations. *ACS Appl. Mater. Interfaces* 7 (42), 23685–23693. doi:10.1021/acsami.5b07517